# SOMA: A New Method to Calculate the Operative Stress Field: Results from the Laurel Mountain Mine, Russell Co., Virginia

**Craig B. Byington,** Senior Geologist - Structural Analysis
Division of Mineral Resources, Commonwealth of Virginia
Big Stone Gap, Virginia, USA

## ABSTRACT

The stress-field orientation mapping and analysis (SOMA) technique for determining the operative stress field near mine workings and its relationship to various fracture sets is described using Dickenson-Russell Coal Company's Laurel Mountain mine as an example. Carried to its practical application, this technique ultimately defines the optimal orientation for the mine workings wherein pillars, rather than rock bolts or other roof support methods, dominantly shoulder support of the highest-probability, potential, roof-fall blocks. It also provides a predictive tool describing local variability in rock deformation and in secondary roof support methods.

Fracture discontinuities within a rock mass, either as pre-existing natural fractures or as mining-induced fractures, are uniquely necessary for every brittle-deformation ground failure including roof falls. Prediction and mitigation of roof falls requires quantifying the interaction between the fracture sets and the operative principal-compressive-stress-axis orientation ($\sigma 1o$). The SOMA technique utilizes the interaction between fractures and $\sigma 1o$, specifically their dilation or closure, to calculate the orientation of $\sigma 1o$, and to estimate the orientations of $\sigma 2o$ and $\sigma 3o$. A stereonet program is used to organize and statistically analyze the fracture data, and then to determine the optimal orientation for the mine workings.

The final step in the SOMA technique involves modeling the Laurel Mountain mine using a 2-D, finite-element, modeling program. This assures that the interpretations regarding the optimal working orientation closely match the deformation features observed in the mine. It also provides a predictive tool describing highly variable stress and strain partitioning, seemingly erratic rock-bolt failures and the interactions between different sets of mine workings within different coal seams. The critical importance of including the fracture sets is well illustrated in the Laurel Mountain mine where the effects of earlier mining of an underlying seam is contrasted in both a fractured and otherwise identical non-fractured model to illustrate the consequences of ignoring fractures in a predictive roof-fall model.

## GENERAL CONCEPT

The loss of, or alternatively the increase of, cohesion and associated ease of shearing along roof, rib and floor fractures reflects the interaction between the fractures and the operative stress field surrounding the mine excavation. Therefore, prediction and mitigation of roof falls require quantifying the interaction between the fracture sets and the operative principal-compressive-stress orientation ($\sigma 1o$).

Only those fractures approximating the operative principal and intermediate stress ($\sigma 1o - \sigma 2o$) plane exhibit significant openings. This results from the relative reduction of the normal stress component as fracture planes approach that orientation. Other fractures oriented orthogonal to $\sigma 1o$ are closed even as those approximately parallel to it are opened. By recognizing that most open fractures share a common $\sigma 1o$, it is possible to plot their mean orientations on a stereonet to determine their common point of intersection, which closely approximates the orientation of $\sigma 1o$. The orientation of the intermediate ($\sigma 2o$) and minimum ($\sigma 3o$) compressive stress axes can also be estimated using this procedure.

As roof fractures are opened they exhibit an undesirable loss of cohesion, decrease in friction and an increased potential for shear-related displacement as compared to the more static closed sets. By comparing the frequency of all fracture set orientations to the calculated $\sigma 1o - \sigma 2o$ plane, those highest probability fall (HPF) fracture combinations can be defined. As the HPF orientations are defined,

the new entry and crosscut excavations can then be reoriented so that both the entries and crosscuts encounter the most frequent HPF fracture sets at the least-acute angle. By crossing the HPF fracture-bounded-block orientation in the shortest distance possible, the length and number of unsupported potential roof-fall blocks are minimized thereby effectively increasing the likelihood that the pillars will assist in the support of potential large roof-fall blocks. In addition, since less is required (decreased loading) of the rock bolts they are more likely to retain the other smaller roof-fall blocks.

Descriptions of the geometric relationships of various fracture types to their respective stress field for both pure and irrotational simple shear have been described by many authors (e.g. Anderson, 1951; Billings, 1972; Ragan, 1973; Sibson, 1977, 1989; Sinclair, 1974 and Sylvester, 1988). Figure 1 schematically illustrates the geometric relationship of fractures with respect to their stress field in a brittle-domain, simple-shear environment. The stress field is shown with orthogonal stress arrows representing the maximum ($\sigma 1$), intermediate ($\sigma 2$) and minimum ($\sigma 3$) stress orientations. Each brittle-domain stress field opens fractures approximating the $\sigma 1$-$\sigma 2$ (extension fracture) plane orientation and tends to close fractures approximating the orthogonal $\sigma 2 - \sigma 3$ orientation. This occurs regardless of the timing, genesis, intensity, frequency or other general characteristics of the fractures; only the orientation and location are important.

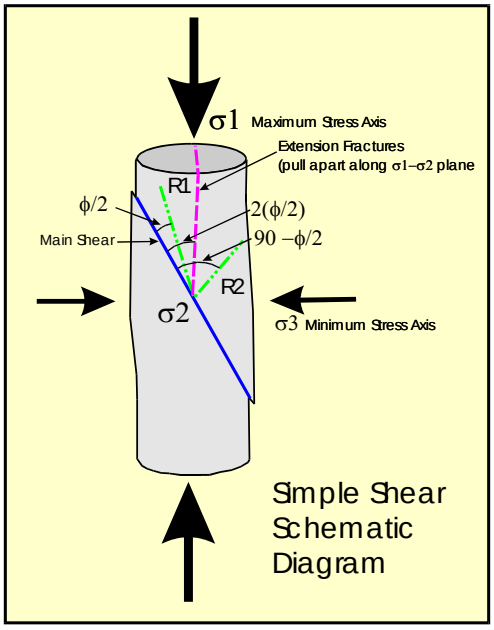


Figure 1 – Schematic diagram of irrotational simple shear showing angular relationships of fracture types with the stress field axes (modified from modified from Ragan, 1973; Sylvester, 1988, and Twiss and Moores, 1992). Riedel shears (R1 and R2) and the coefficient of friction ($\phi$) are shown.

Therefore, by identifying and quantifying open fractures in the mine roof, rib or floor rock, it is possible to calculate the orientation of the stress field that affects the mine workings. More specifically, it is possible to calculate the principal operative stress ($\sigma 1o$) bearing and inclination, which reflects the "warping" of the general stress field by the mine excavation. The calculated $\sigma 1o$ orientation and estimated $\sigma 2o$ and $\sigma 3o$ orientations most correctly apply to the host rock directly adjacent to the mine excavation.

## METHOD

Fracture data was collected from three active but separate areas within the Laurel Mountain mine. By independently calculating the operative stress field for each area, a control check was provided to determine the magnitude of variation in the calculated stress field within the overall area of interest.

To avoid introducing sample bias into the database, all fracture sets were collected irrespective of type or perceived strength, and an effort was made to collect data from both entry and crosscut exposures so that corrective (Terzaghi) weighting would not be necessary. However, fractures with an obvious or suspected local influence on the opening size, such as at yielded pillar corners, were avoided.

Each datum point represents a set of one or more adjacent and similar (type and orientation) fractures. More than 300 fractures measurements were collected and subsequent statistical processing with the stereonet program suggest that this number is sufficient to produce representative results. This database was compiled into a spreadsheet formatted with eight columns. These columns quantify the mean fracture's strike, dip, strength, type, semi-quantitative amount of carbonaceous filling and clay filling, width of opening (millimeters), and general geometric and temporal relationships. However, only the strike, dip, strength and width of opening were used to calculate the operative stress field orientation. The other factors were used to quantify the physical rock parameters in subsequent two dimensional modeling.

In order to organize and statistically process the fracture database, equal-area, lower-hemisphere, stereonet pole plots of each of the fracture groupings were made using DIPS stereonet program (Rocscience, 2002). Each pole represents one or more fracture planes with the same orientation, location and fracture characteristics. The pole plots were contoured through application of Fisher-distribution (spherical statistics) contouring methods with the count-circle size set at 3 percent of the hemisphere surface area. For example, a plot of all open fractures is contoured using a normal-gradient distribution based on the width of fracture openings (Figure 2). A general

clustering of the fracture openings is apparent, but it is also clear that many of the narrower fracture openings (crosses, Figure 2) mask that clustering.

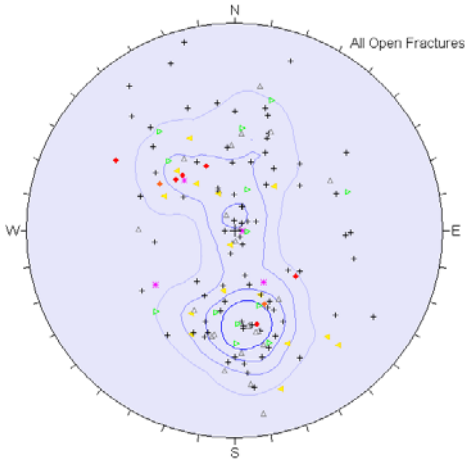


Figure 2 – Contoured stereonet pole plot of all open fractures. Different symbols represent variations in the amount of fracture openings.

The open-fracture widths were plotted as a logarithmic graph (not shown) to define the background and anomalous populations (e.g. see Davis, 1973 and Sinclair, 1974). In this case, the background population is most clearly separated from the anomalous population at a greater-than 2-millimeters opening width. By plotting the data after filtering everything below 3 millimeters, the anomalous-population clustering is more apparent (Figure 3). This clustering indicates a shallow north dipping set, a horizontal set, and a shallow south dipping set of opened fractures. The fracture types include faults, extension fractures and riedel shears in the shallow-dipping sets, and predominantly bedding-plane delaminations in the horizontal set.

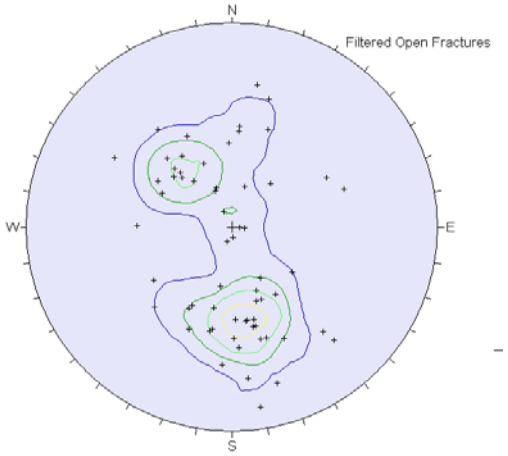


Figure 3 – Contoured stereonet pole plot of open fractures ≥ 3 millimeters. See text for description.

With few exceptions the fractures in the roof, rib and floor are opened or closed as a result of their orientation with respect to the operative stress field. These exceptions generally include local perturbations in the stress field such as near pillar corners, or they may include local areas where the geometry of the mine roof is significantly different, such as at abrupt upward or downward arching in the mine roof.

All open fractures approximate the $\sigma 1_o - \sigma 2_o$ plane and all closed fractures approximate the $\sigma 2_o - \sigma 3_o$ plane. As the open fractures share a common $\sigma 1_o$, they exhibit a common intersection point at $\sigma 1_o$ on the stereonet pole plots. Therefore, by calculating the mean orientation for each of the three open fracture groups (shown as 1m, 2m and 3m great circle arcs in Figure 4) the common intersection point representing $\sigma 1_o$ for the Laurel Mountain mine is established. In this case the calculated $\sigma 1_o$ arrow lies at a bearing of 80° and an inclination of 3° (arrow, Figure 4).

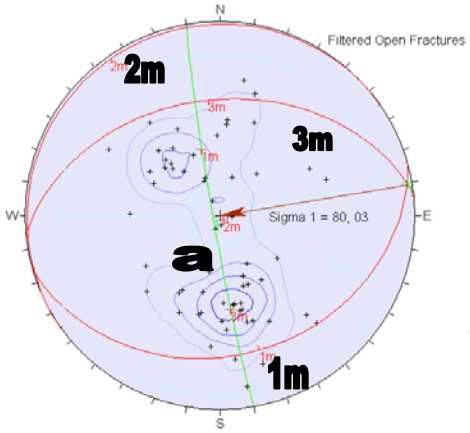


Figure 4 – Stereonet pole plot showing three mean intersecting fracture-set great circles arcs (1m, 2m and 3m). The intersection defines $\sigma 1_o$ (arrow) at a bearing of 80° and an inclination of 3°. See text for descriptions.

Arrows for $\sigma 2_o$ and $\sigma 3_o$ can be estimated by recognizing that fractures do not open if they occur at angles greater than 45° from the $\sigma 1_o - \sigma 2_o$ plane. The plane where all shearing and no extension occurs, the plane of maximum shearing strain, lies at a maximum angle of 45° to $\sigma 1_o$ (or 90° if measured from plane to plane), the direction of maximum normal stress (Figure 5). Angles progressively less than 45° to $\sigma 1_o$ become proportionately more open because they are proportionately less affected by normal stress. By measuring the angular difference between the mean orientations of the two extreme groups (pole crosses marked 1m and 3m), the measured angle of separation is 69° for the acute angle or 111° for the obtuse angle. The $\sigma 1_o - \sigma 2_o$ plane must therefore approximately bisect the acute angle between the two planes at 34 .5° (69°/2 = 34.5°). The acute angle always results in the only permissible angle because it is less than the maximum separation

angle of 90° (45° x 2 = 90°). In other words, the alternative obtuse angle of 111° would yield an unacceptably high bisection angle of 55.5°, considerably higher than the 45° maximum. By assuming that the extension fracture plane is exactly midway between group 1m and group 3m, the results in this case yield a maximum possible error of about 5° ([45-34.5]/2 = ~5).

The first step in computing the orientation of $\sigma_{2o}$ and $\sigma_{3o}$ is completed by constructing a great circle girdle at 90° to $\sigma_{1o}$ (labeled "a", Figure 4). This great circle girdle by definition contains both the $\sigma_{2o}$ and $\sigma_{3o}$ axis. The axis for $\sigma_{3o}$ is found by constructing a friction cone of 34.5° from either of the two mean pole orientations for groups 1m or 3m (circle in northern half of Figure 5). The near-center-of-net intersection of the friction cone with the great circle girdle defines the $\sigma_{3o}$ axis (smallest stress-axis arrow, Figure 5) and the $\sigma_{2o}$ axis (north to south arrow, Figure 5) is located at 90° from that point.

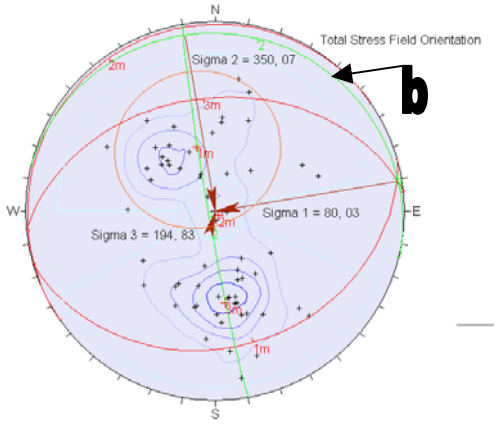


Figure 5 - Stereonet pole plot showing three orthogonal stress axes orientations. See text for descriptions.

The resulting computed bearings and inclinations for the $\sigma_{1o}$, $\sigma_{2o}$ and $\sigma_{3o}$ axes are 80, 03 and 350, 07 and 194, 83, respectively. The $\sigma_{1o} - \sigma_{2o}$ plane (labeled "b", Figure 5) is shallowly inclined, and therefore those fractures with flatter dips such as bedding and low-dip-angle extension fractures are predictably most affected with respect to extensional separation, loss of cohesion and roof failure. This prediction is consistent with field observations where "horse-back" blocks (Figure 6) and bedding-plane delamination (Figure 7) are associated with large and small roof falls at the Laurel Mountain mine.

With a near-vertical $\sigma_{3o}$ (83°), the structural environment at the Laurel Mountain mine is strongly compressional (see Ragan, 1973), and thrust-type shearing is predicted. In addition, those fractures approaching 45° as measured from $\sigma_{1o}$ were predicted to be most affected by shearing forces. As a result of the calculated near horizontal $\sigma_{1o}$, vertical rock bolts penetrating these moderately inclined ($\leq$45°) fractures are predicted as those most likely to fail as a result of shearing strain. This is consistent with field observations by the mine operators where many of the rock bolts and cables were sheared in place, often without an associated roof fall.

Figure 6 – Void in roof where "horse-back" block fell during initial mining at Laurel Mountain mine.

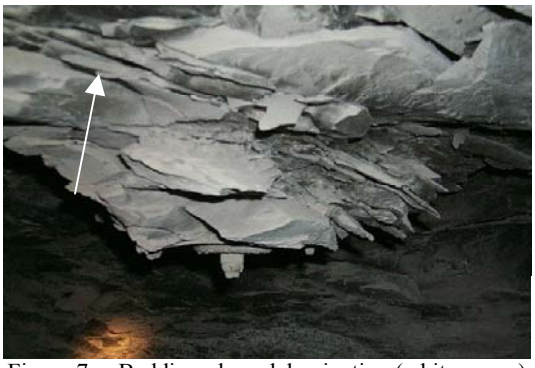

Figure 7 – Bedding plane delamination (white arrow) in roof at Laurel Mountain mine.

## OPTIMAL WORKINGS ORIENTATION

After the stress field was calculated the next step in the SOMA procedure defined the optimal workings orientation. This required that the $\sigma_{1o}$ stress arrow be plotted on a stereonet along with all poles of the mine roof fractures. As previously stated, those fractures approximating the $\sigma_{1o} - \sigma_{2o}$ plane orientation were considered to be the most likely to open and loose cohesion, and as a result, these HPF fractures were the most likely to be involved in roof falls. Therefore the fractures whose orientation occurred within 45° from the $\sigma_{1o} - \sigma_{2o}$ plane were considered to be those most likely to be activated either through extension or shearing. By constructing a 45° friction cone that is perpendicular to the $\sigma_{1o} - \sigma_{2o}$ plane with its pole at $\sigma_{3o}$, the poles of the most likely roof fall fractures are

identified as plotting within the friction cone (Figure 8).

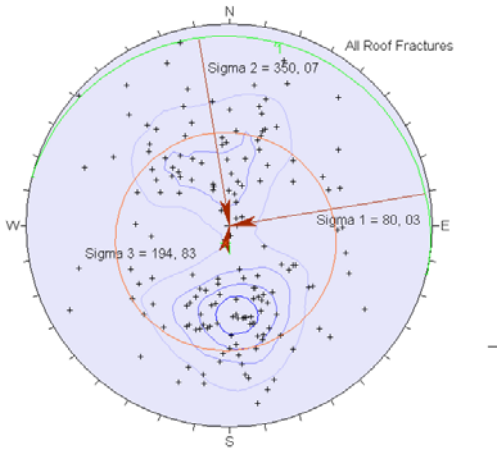


Figure 8 – Contoured stereonet pole plot (n = 333) of all roof fractures and tri-axial stress arrows with friction cone (circle) defining the HPF fracture poles.

It is apparent from the contoured pole plot of all roof fractures that there are two main groups of fractures, some of which fall within the 45° friction cone defining the HPF fractures (Figure 8). These HPF fractures have the greatest probability of being involved in a roof fall because they are the most likely to loose cohesion due to extensional separation and/or shearing. Determining the optimal workings orientation involved considering the probability of occurrence for each fracture orientation. By selecting those most obvious fracture groups, bedding poles at the center of the net neglected for the moment, the great circles for the two groups were defined (Figure 9).

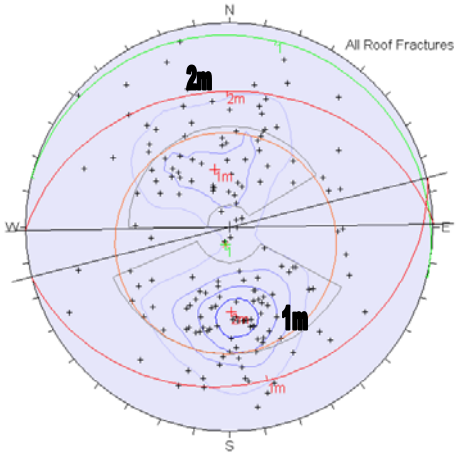


Figure 9 – Contoured stereonet pole plot of all roof fractures showing mean great circles (central arcs) for two most frequent HPF fracture groups and their associated strikes (east-west lines at arc terminations).

The mean orientation (all right-hand rule) for the north dipping and south dipping HPF fracture groups is 76°, 24° (1m, Figure 9) and 269°, 34° (2m Figure 9), respectively. The bedding, measured from a separate stereonet pole plot of all bedding measurements (not shown), is now considered as the third HPF group with its orientation at 126°, 3°. The strike orientations for the two non-bedding groups are calculated (east to west lines Figure 9) at 256° and 269°. Because the two HPF strike orientations are close in this case (256° and 269°), an average of 263° was used.

As excavations driven nearly parallel to the strike of these HPF fractures would excavate the maximum length along the larger roof fall blocks, the SOMA solution indicated that entry and crosscuts be oriented at the greatest bearing angle to those fracture trends. With the entries and crosscuts oriented at 90° to each other, the optimal angle for each heading with respect to the average HPF fracture orientation is approximately 45°. Therefore the optimal workings orientation increased the use of pillars as the main support component for the highest probability roof-fall blocks. This optimal orientation is calculated at 308° (263° + 45° = 308°) for the entry and 218° (263° - 45° = 218°) for the crosscut (Figure 10).

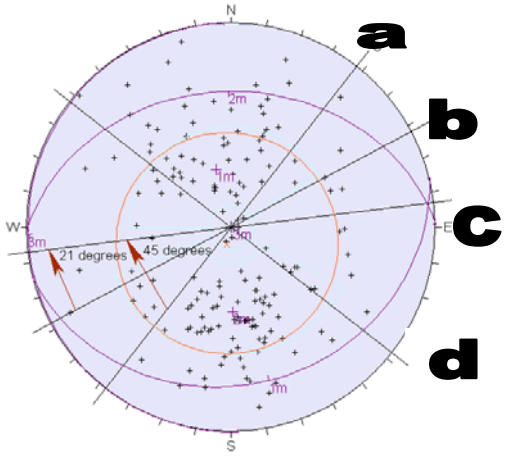


Figure 10 – Stereonet pole plot of all roof fractures showing angular relationships of current and proposed workings bearing with the average HPF fracture bearing. Optimal crosscut bearing (“a” @ 218°), current crosscut bearing (“b” @ 242°), mean HPF fracture orientation (“c” @ 263°) and optimal entry bearing (“d” @ 308°) are shown.

Prior to the SOMA procedure the entry and crosscut bearings were 332° and 242°, respectively. Therefore, although the entry was acceptably oriented at 69° from the average HPF fracture orientation, the crosscut was oriented nearly parallel to that most dangerous orientation at an angle of 21° (Figure 10). The proposed optimal crosscut bearing increases the angle to 45° thereby significantly improving the crosscut angle while effectively sacrificing little in the orientation of the entry. As this solution would predict, field observations confirm that most of the

roof falls in the Laurel Mountain mine occurred in the crosscuts rather than the entries.

## MODELING

After computing the orientations for the operative stress field and the most frequent HPF fractures, a Phase II (Rocscience, 2004) geo-mechanical 2-D model was constructed as the last step in the SOMA procedure. The calculated inclination and bearing of the stress field, measured or published rock-mechanics values and fracture properties (carbonaceous or clay coatings, see Methods), and the roof-support elements were modeled to assure that the deformation characteristics predicted by the 2-D model faithfully recreated the deformation characteristics observed within the Laurel Mountain mine. In addition the magnitude of each stress axes was estimated using published rock mechanics properties (e.g. Molinda and Mark, 1996).

The host-rock strength varies considerably depending on the stress field orientation with respect to sedimentary or structural fabrics such as bedding, or argillaceous, carbonaceous or micaceous laminations, or low-angle fracturing or shearing, (e.g. Molinda and Mark, 1996). As $\sigma_{1o}$ varies in angle to these weakness planes from vertical to horizontal, the operative rock strength approaches either the axial or diametral strength of the rock, respectively. For example, the axial UCS strength is typically at least three times the diametral UCS strength for roof rock (e.g. Molinda and Mark, 1996) illustrating the importance of defining both the bearing and inclination of the stress field with respect to these weakness fabrics.

Features collected in the database, including the characteristics of the fracture surfaces, the fracture's orientation, strength, type, and fracture fillings such as carbonaceous material (typically coal) or clay, were important properties that were factored into the modeling process. For example, clay, coal, and at times, shale were forcibly injected into fractures as a post-diagenetic process within a competent rock type such as sandstone (Figure 11). Each of these late fracture fillings significantly changes the UCS, tensile strength and friction coefficient of the host rock.

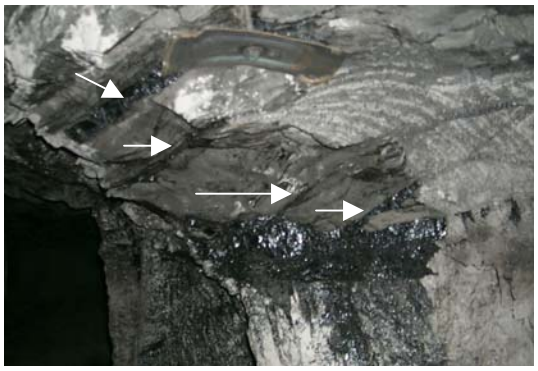

Figure 11 – Coal injections (arrows) into sandstone roof rock. Bedding and coal seam are near horizontal.

The importance of considering the interaction between the fractures and the stress field is well illustrated through the modeling process. In all of the fractured illustrations the roof and floor fracture properties, the rock bolt properties and the fracture properties are representative of those measured in the workings. One model was built with representative fractures while the other model ignored all fractures. Figures 12 through 21 show a vertical cross-section of the Laurel Mountain mine's stratigraphy with a central coal bed (Figures 12-15) or beds (Figures 16-21) separating a sandstone roof from a graywacke floor. Mine excavations are shown as white rectangles. Rock bolts representative of those installed at the mine are shown as vertical lines directly above the excavation. Fractures are shown (Figures 12, 14, 16, 18 & 20) as gray lines terminated with white dots. All model illustrations were contoured on the same contour intervals for comparison.

Partitioning of strain at fracture boundaries is clearly evident in the underground mine exposures. For example, this occurs as variable amounts of post-mining fracture offset in the roof and floor blocks, variability in the amount of rock bolt failure, or as localized compression (roof cutters) or extension (fracture openings, roof falls) features in the roof or floor.

Fracture-based modeling confirmed the underground observations illustrating, by abrupt changes in contour lines and colors, that a significant amount of stress and strain partitioning occurred across fracture boundaries. Local reorientation of the stress axes near the excavations (not shown) was significant. Partitioning of the various strain phenomena, such as total displacement and strength factor were considered in a single-seam, fractured model (Figure 12 and Figure 14) and in a non-fractured model (Figures 13 and 15), respectively

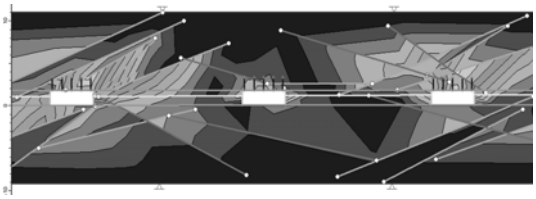

Figure 12 – Single-seam fractured model showing cross-section view of total displacement near crosscuts 3, 4 and 5 (right-left). See text for description. Note partitioning of displacement along fractures. Compare to Figure 13.

When the effects of fracturing are ignored, a simplified model of total displacement is generated that is not consistent with the field observations (Figure 13). Specifically, the non-fractured model results predict a consistent amount of broadly

dispersed deformation in each crosscut, a feature not confirmed in the underground exposures. Neither does the non-fractured model predict the significant amounts of stress partitioning (not shown) that are an obvious feature in the fractured model and suggested by localized shearing of rock bolts.

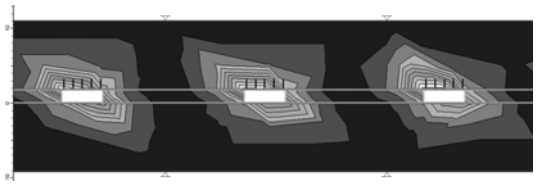

Figure 13 – Single-seam non-fractured model showing cross-section view of total displacement near crosscuts 3, 4 and 5 (right-left). See text for description. Compare to Figure 12.

As a further comparison, the strength factor, which reflects the tensile-strength differential between $\sigma_{1o}$ and $\sigma_{3o}$ in the rock, was computed to contrast the fractured versus non-fractured models. For example, the strength of individual fracture-bounded blocks is often exceeded while that of adjacent blocks in the fractured model is not (Figure 14). However, no such differential is predicted in the otherwise identical non-fractured model (Figure 15).

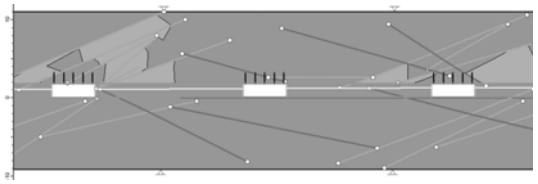

Figure 14 – Single-seam fractured model showing cross-section view of strength factor near crosscuts 3, 4 and 5 (right-left). See text for description. Tensile strength is exceeded (darker gray) in the roof of all three crosscuts. Compare to Figure 15.

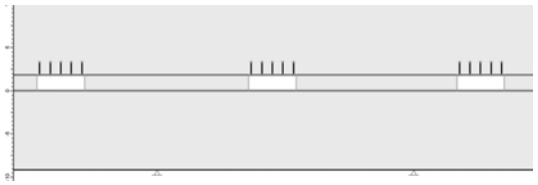

Figure 15 - Single-seam non-fractured model showing cross-section view of strength factor near crosscuts 3, 4 and 5 (right-left). See text for description. Tensile strength is not exceeded in any crosscut. Compare to Figure 14.

Modeling was also completed to predict the effects on ground control of current over-mining of a remnant barrier pillar. These results reflect workings in a 15-meter-distant underlying coal seam that was mined eleven years previously. The solution required quantifying the magnitude and location of the subsidence-related rock failure and predicting roof-control problems resulting from the earlier mining. Again, for comparative purposes the results are presented as both a fractured and non-fractured scenario.

The amount and location of displacement as mining approaches the underlying barrier pillar was addressed with 2-D modeling. When the component of vertical displacement was considered in a fractured model, the results suggested that the negative effects of the underlying barrier pillar would likely be "focused" most intensely in the second crosscut located about 80 meters before the barrier pillar was crossed. Crosscuts three and four, at about 56 and 32 meters from the crossing point, respectively, were predicted to encounter significantly reduced negative effects from that of crosscut two. Crosscuts five and six (~7 and ~–17 meters, respectively) were predicted to experience little or no negative effects (Figure 16).

However when modeling was completed without fractures, a much different scenario was predicted. In this case, the negative effects were not propagated to a particular area as predicted in the fractured model, but rather the predicted effects were dispersed over a much broader zone affecting crosscuts two, three, four and five nearly equally (Figure 17).

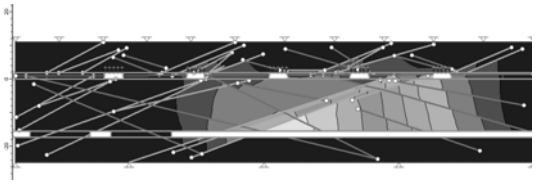

Figure 16 – Double-seam fractured model showing cross-section view of vertical displacement near stage-1 workings (all lower seam excavations), 2, 3, 4, 5 and 6 (right-left, upper seam crosscuts) with fractures (gray lines terminated with white dots). See text for description. Note partitioning of displacement along fractures.

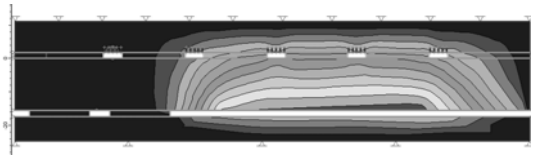

Figure 17 – Double-seam non-fractured model showing cross-section view of vertical displacement near stage-1 workings (all lower seam excavations), 2, 3, 4, 5 and 6 (right-left, upper seam crosscuts). See text for description.

When the tensile strength was computed with both fractured and a non-fractured models, similar differences were apparent. With fractured rock the results confirm considerable variability in the rock strength up to 120 meters from the barrier pillar (Figure 18). The most critical loss of rock strength is predicted to occur near workings located at about a 30° upward projection from the edge of the barrier

pillar in this scenario. As this projection angle is controlled by the inclination of the most-frequent fracture sets, more steeply dipping fractures result in the negative effects being directed upward (or downward) at a steeper angle.

With a non-fractured model the rock's strength factor is not exceeded in any of the crosscuts, although the rock strength is exceeded in the surrounding rock (Figure 19). The non-fractured model predicts that the excavations have de-stressed the roof directly above the crosscut, leading to a sense of security that is not substantiated by past mine experience.

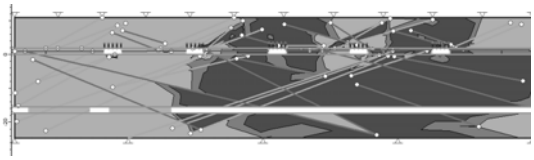

Figure 18 – Double-seam fractured model showing cross-section view of strength factor near stage-1 workings (all lower excavations), 2, 3, 4, 5 and 6 (right-left, upper crosscuts). See text for description. Note partitioning of tensile strength where the rock strength is exceeded (dark gray) to areas where the rock strength is not exceeded (light gray).

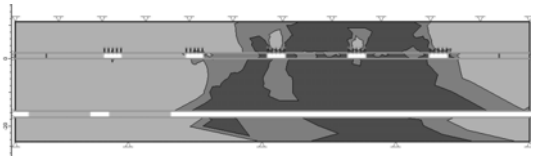

Figure 19 – Double-seam non-fractured model showing cross-section view of strength factor near stage-1 workings (all lower excavations), 2, 3, 4, 5 and 6 (right-left, upper crosscuts). See text for description.

Finally, a comparison (Figures 20 and 21) is made with respect to the movement vectors within the rock when total displacement is considered. With all other parameters remaining consistent in both scenarios the size and direction of the movement vectors are quite different in the two scenarios. In the fractured model with over-mining progressing to the left, it is apparent that the fracture-bounded blocks are being displaced down and to the right in the block overlying the barrier pillar and down and to the left in the block underlying crosscut two (see vector arrows, Figure 20). Significant subsidence is therefore indicated in the number two crosscut while shearing is predicted as the dominant deformation style in crosscuts four, five, and especially three, along fractures dipping down to the left.

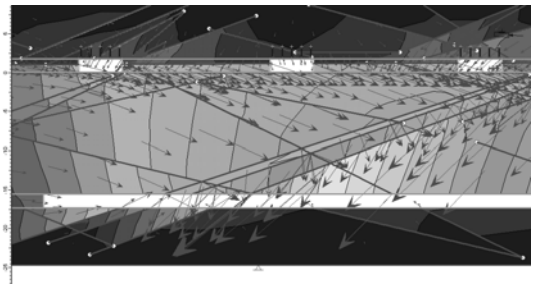

Figure 20 – Double-seam fractured model showing cross-section view of total displacement near stage-1 workings (lower excavations), 3, 4 and 5 (right-left, upper crosscuts). See text for description. Note vector arrows illustrating movement direction and amount (size of arrow). Compare to Figure 21.

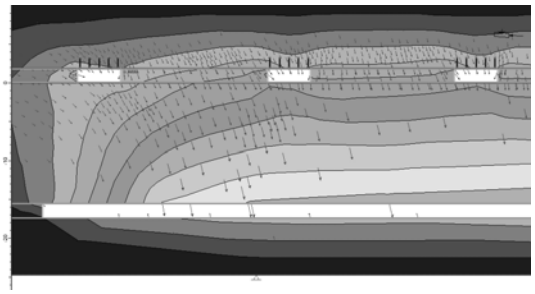

Figure 21 – Double-seam non-fractured model showing cross-section view of total displacement near stage-1 workings (lower crosscuts), 3, 4 and 5 (right-left, upper crosscuts) without fractures. See text for description. Note that vector arrows illustrating that movement direction and amount are considerably smaller and at a much different orientation than in Figure 20.

In the non-fractured model (Figure 21) the predicted amount of displacement is significantly less (compare to Figure 20) as is indicated by the size of the displacement vectors (arrows). In this scenario the direction of displacement is exclusively downward and slightly to the right. This model does not predict the significant differences in the amount of displacement from area to area that is registered in the mine workings, nor does it predict the measured amounts of shearing exposed in local areas.

## CONCLUSIONS

Fractures are uniquely involved in every roof fall (versus roof sag) and they occur either as pre-existing, generally tectonic induced discontinuities, or as subsequent mining-induced discontinuities. As such they are unquestionably important in understanding and predicting roof-fall behavior, and more importantly, mitigating roof fall occurrences.

However, fractures alone do not fully explain roof fall behavior. Fracture considerations based on the type, frequency, intensity of deformation or genesis

fail to adequately explain roof fall occurrences. Indeed, there are many fracture orientations that are infrequently or never involved in roof falls within a particular mine while other fracture sets are frequently or always involved. Observations made in the mine workings, laboratory testing ( UCS testing) and subsequent 2-D modeling consistently document that fractures occurring at certain orientations, specifically those approaching the $\sigma_{1o}$- $\sigma_{2o}$ plane open and are involved in roof falls. Therefore the need to accurately measure the operative stress field's orientation(s) is requisite in accurately predicting roof-, rib- and floor-rock behavior.

The SOMA technique allows the operative stress field to be calculated by measuring the amount of deformation produced, in this case through opening of fracture planes, by the operative stress field. By defining the bearing and inclination of $\sigma_{1o}$ and estimating the bearing and inclination of $\sigma_{2o}$ and $\sigma_{3o}$, the interaction between the fractures and the stress field can be accurately quantified. Those fractures that are affected by the stress field are identified by the SOMA technique.

Determining the optimal working orientation involves an additional step. The probability of each set of HPF fractures being involved in a roof fall was also considered. The end result of this work prescribed an orientation for the crosscuts and entries that resulted in additional pillar support of the most-likely-to-fall blocks. Post-SOMA results document that as the pillars supported more of the potential fall blocks, particularly the larger fall blocks, roof fall frequency in the Laurel Mountain mine decreased and the performance of secondary support techniques such as rock bolts and crib sets is predicted to improve.

Two-dimensional modeling was performed to check the results of the SOMA technique and predict where, the style and to what relative magnitude the fracturing will cause roof-fall failures. Models were calculated for both a fractured and a non-fractured scenario. This modeling reaffirms that when fractures are not considered, a misleading, at best, and potentially dangerous, at worst, predictive model results. For example, very strong stress and strain partitioning was evident in the fractured model whereas the non-fractured model suggested a wider, more homogeneous distribution of the stress and strain differentials. Local but distinct changes of the rock strength and the movement vectors in the fractured scenario warned of local roof-fall blocks and local shear failure in bolts penetrating moderately dipping fractures at these locations. The non-fractured model failed to accurately predict any of the significant roof-, floor- or rib-deformation features.

When the fractured and non-fractured models were constructed for an over-mining scenario, similar shortcomings were evident in the non-fractured model. Results indicate that as a result of stress/strain partitioning, potentially dangerous roof conditions could be encountered well before that predicted using a non-fractured model. Fractured model results reveal that the effects of crossing a barrier pillar could be propagated to workings over 80 meters from the point directly above the barrier pillar. The non-fractured model in contrast predicted that no potentially dangerous changes would be encountered as the barrier pillar was crossed.

In all cases these results argue that for geo-mechanical solutions to be representative and useful as predictive tools, then the interaction between the fractures and the stress field must be considered. As there are obvious and discrete fracture discontinuities in the rock mass, it is requisite that those discontinuities be considered in successful modeling.

## REFERENCES


Anderson, E.M., *The Dynamics of Faulting:* 2nd ed., Edinburg, Oliver and Boyd, 1951, 206 p.

Billings, M.D., *Structural Geology*: Prentice-Hall, Englewood Cliffs, New J., 1972, p. 168-169.

Davis, J. C., *Statistics and Data Analysis in Geology*: John Wiley and Sons, New York, New York, 1973, 550 p.

Rocscience, Inc., 1989-2002, Dips, Release 5.075, Rock Engineering Group, University of Toronto; Toronto, Ontario, Canada.

McKinstry, H.E., *Mining Geology*: New Jersey, Prentice-Hall, Inc., 1948, p. 290-327.

Molinda, G.M., and Mark, C., Rating the strength of coal mine roof rocks, USBM IC 9387, 1996, 36 pp.

Rocscience, Inc., 1999-2004, Phase II, Release 5.044, Rock Engineering Group, University of Toronto; Toronto, Ontario, Canada.

Ragan, D.M., *Structural Geology, An Introduction to Geometrical Techniques*: John Wiley and Sons, 2nd ed., 1973, 208 p.

Sibson, R.H., Fault rocks and fault mechanisms: Journal of the Geological Society of London, 133, 1977, p. 191-213.

Sibson, R.H., Structure and mechanics of fault zones in relation to fault-hosted mineralization: Australian Mineral Foundation, Adelaide, Australia, 1989, 66 p.

Sinclair, A.J., Selection of thresholds in geochemical data using probability graphs: Journal of Geochemical Exploration, v. 3, 1974, p. 129-149.

Sylvester, A.G., Strike-slip faults: Geological Society of America Bulletin, v. 100, 1988, p. 1666-1703.

Twiss, R.J., and Moores, E.M., *Structural Geology*: W. H. Freeman and Company, New York, New York, 1992, 532 p.